AD

TECHNICAL REPORT ARBRL-TR-02532

NAVIER-STOKES COMPUTATIONS OF PROJECTILE BASE FLOW AT TRANSONIC SPEEDS WITH AND WITHOUT BASE INJECTION

Jubaraj Sahu
Charles J. Nietubicz
J. L. Steger

November 1983

US ARMY ARMAMENT RESEARCH AND DEVELOPMENT CENTER
BALLISTIC RESEARCH LABORATORY
ABERDEEN PROVING GROUND, MARYLAND

Destroy this report when it is no longer needed.
Do not return it to the originator.

Additional copies of this report may be obtained from the National Technical Information Service, U. S. Department of Commerce, Springfield, Virginia 22161.

The findings in this report are not to be construed as an official Department of the Army position, unless so designated by other authorized documents.

The use of trade names or manufacturers' names in this report does not constitute indorsement of any commercial product.

UNCLASSIFIED

SECURITY CLASSIFICATION OF THIS PAGE *(When Data Entered)*

REPORT DOCUMENTATION PAGE		READ INSTRUCTIONS BEFORE COMPLETING FORM
1. REPORT NUMBER TECHNICAL REPORT ARBRL-TR-02532	2. GOVT ACCESSION NO.	3. RECIPIENT'S CATALOG NUMBER
4. TITLE *(and Subtitle)* NAVIER-STOKES COMPUTATIONS OF PROJECTILE BASE FLOW AT TRANSONIC SPEEDS WITH AND WITHOUT BASE INJECTION		5. TYPE OF REPORT & PERIOD COVERED Final 6. PERFORMING ORG. REPORT NUMBER
7. AUTHOR(s) J. Sahu, C. J. Nietubicz, & J. L. Steger*		8. CONTRACT OR GRANT NUMBER(s)
9. PERFORMING ORGANIZATION NAME AND ADDRESS U.S. Army Ballistic Research Laboratory, ARDC ATTN: DRDAR-BLL(A) Aberdeen Proving Ground, Maryland 21005		10. PROGRAM ELEMENT, PROJECT, TASK AREA & WORK UNIT NUMBERS RDT&E 1L161102AH43
11. CONTROLLING OFFICE NAME AND ADDRESS US Army AMCCOM, ARDC Ballistic Research Laboratory, ATTN: DRSMC-BLA-S(A) Aberdeen Proving Ground, MD 21005		12. REPORT DATE November 1983 13. NUMBER OF PAGES 39
14. MONITORING AGENCY NAME & ADDRESS*(if different from Controlling Office)*		15. SECURITY CLASS. *(of this report)* UNCLASSIFIED 15a. DECLASSIFICATION/DOWNGRADING SCHEDULE

16. DISTRIBUTION STATEMENT *(of this Report)*

Approved for public release; distribution unlimited.

17. DISTRIBUTION STATEMENT *(of the abstract entered in Block 20, if different from Report)*

18. SUPPLEMENTARY NOTES

*Stanford University
Department of Aeronautics and Astronautics
ATTN: Prof. J. L. Steger
Stanford, CA 94305

19. KEY WORDS *(Continue on reverse side if necessary and identify by block number)*

Base Flow
Transonic Speeds
Base Bleed
Projectile Aerodynamics
Navier-Stokes Computations
Base Pressure
Drag Components
Computational Fluid Dynamics

20. ABSTRACT *(Continue on reverse side if necessary and identify by block number)*

A computational capability has been developed for predicting the flow field about the entire projectile, including the recirculatory base flow, at transonic speeds. Additionally, the computer code allows mass injection at the projectile base and hence is used to show the effects of base bleed on base drag. Computations have been made for a secant-ogive-cylinder projectile for a series of Mach numbers in the transonic flow regime. Computed results show the qualitative and quantitative nature of base flow with and without

DD FORM 1 JAN 73 1473 EDITION OF 1 NOV 65 IS OBSOLETE

UNCLASSIFIED

SECURITY CLASSIFICATION OF THIS PAGE *(When Data Entered)*

20. ABSTRACT (Continued)

base bleed. The reduction in base drag with base bleed is clearly predicted for various mass injection rates and for Mach numbers $.9 < M < 1.2$. The encouraging results obtained indicate that this computational technique may provide useful design guidance for shell with base bleed.

TABLE OF CONTENTS

This page Left Intentionally Blank

LIST OF ILLUSTRATIONS

This page Left Intentionally Blank

I. INTRODUCTION

A major area of concern in shell design is the total aerodynamic drag. The designer, ever desirous of increasing the range and/or terminal velocity of projectiles, is eager to decrease the aerodynamic drag.

The total drag of projectiles can be divided into three components: (1) pressure drag (excluding the base region), (2) viscous (skin friction) drag, and (3) base drag. For a typical shell at M = .90 the relative magnitudes of the aerodynamic drag components are: (1) pressure drag, 20%, (2) viscous drag, 30%, and (3) base drag, 50%. The pressure and viscous components generally cannot be reduced significantly without adversely affecting the stability of shell. Recent attempts to reduce the total drag are therefore directed at reducing the base drag.

A number of studies have been made to examine the total drag reduction due to the addition of a boattail. Although this is very effective in reducing the total drag, it has a negative impact on the aerodynamic stability of shell especially at transonic velocities. An excellent review of the effect of boattailing on total drag and base pressure is presented in Reference 1.

Another effective means of reducing the base drag is that of 'base bleed' or 'base injection.' In this method, a small amount of mass is injected into the base region which increases the base pressure and thus reduces the base drag. Recent range and precision tests[2] of a 155mm projectile with and without base bleed have been conducted and an 85% reduction in base drag was obtained. Presently the XM864 is an active projectile design which is attempting to use the base bleed concept for increased range. This concept of mass injection at the projectile base has been widely studied for supersonic flows and much of the work has been reported in Reference 3. One limited study at supersonic speeds was made at BRL and the results were reported by Dickinson.[4] The supersonic regime has typically been the area where increased range due to

---

1. *Sedney, R., "Review of Base Drag," Report No. 1337, U.S. Army Ballistic Research Laboratory, Aberdeen Proving Ground, Maryland, 21005, October 1966 (AD 808767).*

2. *"155mm ERFB Base Bleed Range and Precision Tests," Conducted at Proof and Experimental Test Establishment, Nicolet, Quebec, for Space Research Corporation, January 11, 1978.*

3. *Murthy, S.N.B. (Ed.), "Progress in Astronautics and Aeronautics: Aerodynamics of Base Combustion," Vol. 40, AIAA, New York, 1976.*

4. *Dickinson, E.R., "The Effectiveness of Base-Bleed in Reducing Drag of Boattailed Bodies at Supersonic Velocities," Memorandum Report No. 1244, U.S. Army Ballistic Research Laboratory, Aberdeen Proving Ground, Maryland 21005, 1960 (AD 234315).*

drag reduction has been studied. Thus, only limited attention has been focussed on the 'base bleed' problem in transonic flow. A limited study made in the transonic flow regime has been reported in Reference 5 which describes the effects of base bleed on various afterbody configurations.

Most of the work using the 'base bleed' concept has been either experimental or semi-empirical in nature. Sophisticated numerical techniques have not yet been utilized to predict the effects of base bleed on the base drag reduction. Limited computational work was reported recently by Sullins, et al.[6] Their work dealt with the numerical computation of the base region flow of a supersonic combustion ramjet engine using two-dimensional Navier-Stokes equations. They computed the flow field in the vicinity of the base with parallel gas injection and established the effect of base injection on such flows.

Because of the recent advances in computer technology, numerical computational capabilities have been developed to predict the aerodynamic behavior of artillery shell. Recent papers[7,8] have reported the development and application of the Azimuthal-Invariant Thin-Layer Navier-Stokes computational technique to predict the flow about slender bodies of revolution at transonic speeds. This technique has been modified for base flow analysis and the resulting new numerical capability[9] is used here to predict the base pressure of shell at transonic speeds including the effect of base bleed. Computed results show quantitative and qualitative details of the base flow structure. The technique computes the full flow field over the projectile at transonic speeds; therefore, all three components of the total drag (pressure, viscous, and base drag) are computed. This computational technique is then applied to predict the effects of base bleed on the base drag reduction at transonic

---

5. *Sykes, D.M., "Cylindrical and Boattailed Afterbodies in Transonic Flow with Gas Ejection," AIAA Journal, Vol. 8, No. 3, March 1970, pp. 588-589.*

6. *Sullins, G.A., Anderson, J.D., and Drummond, J.P., "Numerical Investigation of Supersonic Base Flow with Parallel Injection," AIAA Paper No. 82-1001, June 1982.*

7. *Nietubicz, C.J., Pulliam, T.H., and Steger, J.L., "Numerical Solution of the Azimuthal-Invariant Thin-Layer Navier-Stokes Equations," ARBRL-TR-02227, U.S. Army Ballistic Research Laboratory, Aberdeen Proving Ground, Maryland 21005, March 1980 (AD A085716).*

8. *Nietubicz, C.J., "Navier-Stokes Computations for Conventional and Hollow Projectile Shapes at Transonic Velocities," ARBRL-MR-03184, U.S. Army Ballistic Research Laboratory, Aberdeen Proving Ground, Maryland 21005, July 1982 (AD A116866).*

9. *Sahu, J., Nietubicz, C.J., and Steger, J.L., "Numerical Computation of Base Flow for a Projectile at Transonic Speeds," ARBRL-TR-02495, U.S. Army Ballistic Research Laboratory, Aberdeen Proving Ground, Maryland 21005, June 1983 (AD A130293).*

speeds. The combined effect of boattailing and base bleed is, however, not considered in this report.

Brief descriptions of the physical problem and the governing equations are given in Sections II and III, respectively. The computational technique and the method of solution are discussed in Section IV. In Section V, results are shown for transonic base pressure computations for a 6-caliber secant-ogive-cylinder shape for $.9 < M < 1.2$, with and without base bleed. Velocity vector plots and stream function contour plots are presented to show the qualitative features of the flow field in the base region. Quantitative comparisons of base drag and the total drag, both with and without base injection, have been made. The encouraging results show that the present computational technique can be used to study the effects of base bleed on base drag and thus can have a positive impact on the XM864 devleopment. Although results in this report are presented for transonic speeds, current computational efforts are directed at supersonic velocities.

II. PHYSICAL PROBLEM

The physical problem deals with the transonic flow over a projectile, including the base region. Although the entire projectile flow is computed, the emphasis is on the flow field in the base region of the projectile. A small amount of air is injected at the projectile base in the direction parallel to the primary flow. The injection at the base can be concentrated at the center of the base or spread throughout the entire base. In the present work, however, the injection takes place over 90% of the base. Figure 1 shows a schematic illustration of the base region flow field with base injection. The dividing streamline separates the recirculary base flow from the primary external flow. The flow field is dominated by separation and mixed regions of locally supersonic and subsonic flows.

The complete set of time-dependent generalized axisymmetric thin-layer Navier-Stokes equations is solved to obtain a numerical solution to this problem. The numerical technique used is an implicit finite-difference scheme. Although time-dependent calculations are made, the transient flow is not of primary interest at the present time. The steady flow is the desired result which is obtained in a time asymptotic fashion.

III. GOVERNING EQUATIONS

The Azimuthal Invariant (or Generalized Axisymmetric) thin-layer Navier-Stokes equations for general spatial coordinates ξ, η, ζ can be written as[7]

$$\frac{\partial \hat{q}}{\partial \tau} + \frac{\partial \hat{E}}{\partial \xi} + \frac{\partial \hat{G}}{\partial \zeta} + \hat{H} = Re^{-1} \frac{\partial \hat{S}}{\partial \zeta} \tag{1}$$

where $\xi = \xi(x,y,z,t)$ is the longitudinal coordinate

$\eta = \eta(y,z,t)$ is the circumferential coordinate

$\zeta = \zeta(x,y,z,t)$ is the near normal coordinate

$\tau = t$ is the time

The vector of dependent variables $\hat{q}$ and the flux vectors $\hat{E}$, $\hat{G}$, $\hat{H}$ are given as

$$\hat{q} = J^{-1} \begin{bmatrix} \rho \\ \rho u \\ \rho v \\ \rho w \\ e \end{bmatrix}, \qquad \hat{E} = J^{-1} \begin{bmatrix} \rho U \\ \rho u U + \xi_x p \\ \rho v U + \xi_y p \\ \rho w U + \xi_z p \\ (e + p) U - \xi_t p \end{bmatrix}$$

$$\hat{G} = J^{-1} \begin{bmatrix} \rho W \\ \rho u W + \zeta_x p \\ \rho v W + \zeta_y p \\ \rho w W + \zeta_z p \\ (e + p) W - \zeta_t p \end{bmatrix},$$

$$\hat{H} = J^{-1}\phi_\eta \begin{bmatrix} 0 \\ 0 \\ \rho V[R_\xi(U - \xi_t) + R_\zeta(W - \zeta_t)] \\ -\rho V R \phi_\eta (V - \eta_t) - p/(R\phi_\eta) \\ 0 \end{bmatrix}$$

where J is the Jacobian of transformation.

The thin layer viscous terms valid for high Reynolds number flow are contained in the vector $\hat{S}$, where

$$\hat{S} = \begin{bmatrix} 0 \\ \mu(\zeta_x^2 + \zeta_y^2 + \zeta_z^2)u_\zeta + (\mu/3)(\zeta_x u_\zeta + \zeta_y v_\zeta + \zeta_z w_\zeta)\zeta_x \\ \mu(\zeta_x^2 + \zeta_y^2 + \zeta_z^2)v_\zeta + (\mu/3)(\zeta_x u_\zeta + \zeta_y v_\zeta + \zeta_z w_\zeta)\zeta_y \\ \mu(\zeta_x^2 + \zeta_y^2 + \zeta_z^2)w_\zeta + (\mu/3)(\zeta_x u_\zeta + \zeta_y v_\zeta + \zeta_z w_\zeta)\zeta_z \\ \{(\zeta_x^2 + \zeta_y^2 + \zeta_z^2)[0.5\mu(u^2 + v^2 + w^2)_\zeta + \kappa Pr^{-1}(\gamma - 1)^{-1}(a^2)_\zeta] \\ \quad + (\mu/3)(\zeta_x u + \zeta_y v + \zeta_z w) \times (\zeta_x u_\zeta + \zeta_y v_\zeta + \zeta_z w_\zeta)\} \end{bmatrix}$$

The velocities

$$U = \xi_t + \xi_x u + \xi_y v + \xi_z w$$
$$V = \eta_t + \eta_x u + \eta_y v + \eta_z w \qquad (2)$$
$$W = \zeta_t + \zeta_x u + \zeta_y v + \zeta_z w$$

represent the contravariant velocity components.

The Cartesian velocity components (u, v, w) are nondimensionalized with respect to a_∞ (the free stream speed of sound). The density (ρ) is referenced to ρ_∞ and total energy (e) to $\rho_\infty a_\infty^2$. The local pressure is determined using the equation of state,

$$p = (\gamma - 1)[e - 0.5\rho(u^2 + v^2 + w^2)] \qquad (3)$$

where γ is the ratio of specific heats.

In Equation (1) a thin-layer approximation is used and the restrictions for axisymmetric flow are imposed. The details can be found in References 8 and 9 and are not discussed here. Equation (1) contains only two spatial derivatives; however, it retains all three momentum equations, thus allowing a degree of generality over the standard axisymmetric equations. In particular, the circumferential velocity is not assumed to be zero, thus allowing computations for spinning projectiles or swirl flow to be accomplished. There is some evidence which indicates that base pressure can change due to the spin of a projectile. Although the present work considers base flow with no spin, base flow with spin is of interest and can be studied using the present technique.

For the computation of turbulent flows a turbulence model must be supplied. In the present calculations a Cebeci-type two layer algebraic eddy viscosity model as modified by Baldwin and Lomax[10] is used. In their two layer model the inner region follows the Prandtl-Van Driest formulation. Their outer formulation can be used in wakes as well as in attached and separated boundary layers. In both the inner and outer formulations the distribution of vorticity is used to determine length scales, thereby avoiding the necessity of finding the outer edge of the boundary layer (or wake). The magnitude of the local vorticity for the axisymmetric formulation is given by

$$|\omega| = \sqrt{\left(\frac{\partial v}{\partial x}\right)^2 + \left(\frac{\partial v}{\partial z} - \frac{\partial w}{\partial y}\right)^2 + \left(\frac{\partial w}{\partial x} - \frac{\partial u}{\partial z}\right)^2} \qquad (4)$$

---

10. *Baldwin, B.S., and Lomax, H., "Thin-Layer Approximation and Algebraic Model for Separated Turbulent Flows," AIAA Paper No. 78-257, 1978.*

In determining the outer length scale a function[10]

$$F(y) = y|\omega| \left[1 - \exp(-y^+/A^+)\right] \tag{5}$$

is used where y^+ and A^+ are the conventional boundary layer terms. For the base flow (or wake flow) the exponential term of Equation (5) is set equal to zero.

IV. NUMERICAL METHOD

A. Computational Algorithm

An implicit, approximate factorization, finite-difference scheme in delta form as described by Beam and Warming[11] is used. An implicit method was chosen because it permits a time step much greater than that allowed by explicit schemes. For problems in which the transient solution is of no interest, this offers the advantage of being able to reach the steady state solution faster than existing explicit schemes.

The Beam-Warming implicit algorithm has been used successfully in various applications.[7-13] The algorithm can be first or second order accurate in time and second or fourth order accurate in space. The equations are factored (spatially split) which reduces the solution process to one-dimensional problems at a given time level. Central difference operators are employed and the algorithm produces block tridiagonal systems for each space coordinate. The main computational work is contained in the solution of these block tridiagonal systems of equations.

---

11. *Beam, R., and Warming, R.F., "An Implicit Factored Scheme for the Compressible Navier-Stokes Equations," AIAA Journal, Vol. 16, No. 4, April 1978, pp. 393-402.*

12. *Steger, J.L., "Implicit Finite Difference Simulation of Flow About Arbitrary Geometries with Application to Airfoils," AIAA Journal, Vol. 16, No. 7, July 1978, pp. 679-686.*

13. *Pulliam, T.H., and Steger, J.L., "On Implicit Finite-Difference Simulations of Three-Dimensional Flow," AIAA Journal, Vol. 18, No. 2, February 1980, pp. 159-167.*

B. Finite Difference Equations

The resulting finite difference equations, written in delta form are

$$(I + h\delta_\xi \hat{A}^n - \varepsilon_I J^{-1}\nabla_\xi \Delta_\xi J)(I + h\delta_\zeta \hat{C}^n - \varepsilon_I J^{-1}\nabla_\zeta \Delta_\zeta J$$

$$- hRe^{-1}\delta_\zeta J^{-1}\hat{M}^n J)\ (\hat{q}^{n+1} - \hat{q}^n) = -\Delta t(\delta_\xi \hat{E}^n + \delta_\zeta \hat{G}^n \qquad (6)$$

$$-Re^{-1}\delta_\zeta \hat{S}^n) - \Delta t\hat{H}^n - \varepsilon_E J^{-1}[(\nabla_\xi \Delta_\xi)^2 + (\nabla_\zeta \Delta_\zeta)^2]J\hat{q}^n$$

Here $h = \Delta t$ because only first order accuracy in the time differencing is needed for the steady state flows considered here. This choice corresponds to the Euler implicit time differencing. The δ's represent central difference operators, Δ and ∇ are forward and backward difference operators, respectively. The Jacobian matrices $\hat{A} = \frac{\partial \hat{E}}{\partial q}$, $C = \frac{\partial \hat{G}}{\partial q}$ together with the coefficient matrix $\hat{M}$ obtained from the local time linearization of $\hat{S}$ are described in detail in Reference 6. Fourth order explicit (ε_E) and implicit (ε_I) numerical dissipation terms are incorporated into the differencing scheme to damp high frequency growth and thus to control the nonlinear instabilities. A typical range for the smoothing coefficients is ε_E = (1 to 5) Δt with $\varepsilon_I = 3\varepsilon_E$.

C. Flow Field Segmentation

Figure 2 is a schematic illustration of the flow field segmentation used to compute the entire projectile flow field including the base flow. It shows the transformation of the physical domain into the computational domain and the details of the flow field segmentation procedure in both domains.

The cross hatched region represents the projectile. The line BC is the projectile base and the region ABCD is the base region or the wake. The line AB is a computational cut through the physical wake region which acts as a repetitive boundary in the computational domain. Implicit integration is carried out in both ξ and ζ directions. (See Figure 2.) Note the presence of the lines BC (the base) and EF (nose axis) in the computational domain. They both, however, act as boundaries in the computational domain and special care must be taken in forming the block tridiagonal matrix in the ξ direction. The details are presented in the next section.

D. Implementation of Boundary Conditions

1. Base Flow without Base Injection.

The no-slip boundary conditions for viscous flow are enforced by setting

$$U = V = W = 0 \tag{7}$$

on the projectile surface except for the base. At the projectile base the velocity component normal to the base is set to zero, i.e., $U = 0$, while other flow variables are set equal to those at grid point next to the base.

Along the computational cut (line AB), the flow variables above and below the cut were simply averaged to determine the boundary conditions on the cut. On the centerline of the wake region, a symmetry condition is imposed:

$$\begin{aligned} \frac{\partial u}{\partial z} &= 0 \\ \frac{\partial v}{\partial z} &= 0 \\ w &= 0 \\ \frac{\partial p}{\partial z} &= 0 \end{aligned} \tag{8}$$

Free stream conditions are used at the outer boundary. First order extrapolation for all flow variables is used at the downstream boundary (lines AD and AG). During transient calculations, use of a specified outflow pressure can give rise to numerical oscillations in the base region flow field. Eventually, these grow and swamp the solution. This difficulty is avoided by simply extrapolating pressure to the downstream boundary which is the procedure always used with supersonic outflow. A combination of extrapolation and symmetry is used on the nose axis (line EF).

As a result of the flow field segmentation procedure described earlier, the block tridiagonal matrix in the ξ direction has elements at J = JB, JB+1 which are treated as internal boundaries in the computational domain. (J = JB represents the projectile base and J = JB+1 is the nose axis.) The block tridiagonal matrix in the ξ direction takes the following form (after setting $\epsilon_I = 0$ to simplify the illustration)

$$
\begin{bmatrix}
I & A_3 & & & & & \\
-A_2 & I & A_4 & & & & \\
 & \ddots & \ddots & \ddots & & & \\
 & & -A_{JB-2} & I & A_{JB} & & \\
 & & & 0 & I & 0 & \\
 & & & & 0 & I & 0 \\
 & & & -A_{JB+1} & I & A_{JB+3} & \\
 & & & & \ddots & \ddots & \ddots \\
 & & & & & -A_{JMAX-2} & I
\end{bmatrix}^n
\begin{bmatrix}
\Delta q_2 \\ \Delta q_3 \\ \vdots \\ \Delta q_{JB} \\ \Delta q_{JB+1} \\ \vdots \\ \Delta q_{JMAX-1}
\end{bmatrix}^n
=
\begin{bmatrix}
RHS_2 \\ RHS_3 \\ \vdots \\ 0 \\ 0 \\ \vdots \\ RHS_{JMAX-1}
\end{bmatrix}^n
\qquad (9)
$$

Here A's denote the quantity $\frac{\Delta t}{2\Delta\xi}\hat{A}$ and I is a 5x5 identity matrix. Note the appearance of two uncoupled block tridiagonals. The rows at JB and JB+1 are particularly simple because boundary conditions are updated explicitly at the end of inversions. These changes were easily implemented in a modular fashion into an existing code for projectile base flow computations. One simply fills the block tridiagonal matrix ignoring the base JB and the nose axis JB+1. Elements in these rows are then overloaded as shown above. The flow field segmentation does not affect the block tridiagonal matrix in the ζ direction.

2. Base Flow with Base Injection.

The boundary conditions used for base flow with mass addition are presented here. The boundary conditions along the projectile surface, at the cut and downstream boundary all remain the same as previously described. Along the base boundary the following conditions are imposed:

$$u = u_j$$

$$v = v_j = 0$$

$$w = w_j = w_{JB-1} \text{ (grid point next to the base)}$$

$$\rho = \rho_j = \rho_{st}$$

The stagnation density is obtained from the following relation.

$$\frac{p_{st}}{p_\infty} = \left(1 + \frac{\gamma-1}{2} M_\infty^2\right)^{\frac{1}{\gamma-1}} \qquad (10)$$

The amount of air injected into the base region can be specified by the mass flow rate, $\dot{m}_j$. Since ρ_j and A_j are known, u_j can be calculated for any given mass flow rate. Rather than specifying $\dot{m}_j$, however, it is customary to specify a mass injection parameter, I_j where $I_j = \dot{m}_j/\rho_\infty u_\infty A$. Most of the results with base bleed are presented in terms of this parameter in the next section. It is important to remember that the smaller the mass injection parameter, the smaller is the amount of mass injected at the base.

E. Computational Grid

The finite difference grid used for the numerical computations was obtained from a grid generator developed and reported in Reference 14. This program allows arbitrary grid point clustering, thus enabling grid points for the projectile shapes to be clustered in the vicinity of the body surface. The grid consists of 108 points in the longitudinal direction and 50 points in the radial direction. The full grid is shown in Figure 3 while Figure 4 shows an expanded view of the grid in the vicinity of the projectile. The computational domain extended to 4 body lengths in front, 4 body lengths in the radial direction and 4 body lengths behind the base of the projectile. The grid points in the normal direction were exponentially stretched away from the surface with the minimum spacing at the wall of .00002D. This spacing locates at least two points within the laminar sublayer.

The grid shown in Figure 4 was generated in two segments. First, the grid in the outer region is obtained using an elliptic solver[14] for the ogive portion and straight-line rays for the remaining portion which runs all the way to downstream boundary. Second, the grid in the base region is obtained simply by extending the straight lines perpendicular to line AB down to the center line of symmetry (line CD). An exponential stretching with the minimum spacing of .00002D at line AB is used. It should be noted that the same minimum spacing .00002D is specified on both sides of the cut thus maintaining a smooth variation of grid across the cut. This spacing could, of course, be increased downstream of the base. The number of grid points above and below line AB is the same (50 points). As can be seen in Figure 4, the grid points are clustered near the nose-cylinder junction and at the projectile base where appreciable changes in flow variables are expected.

As indicated in Figure 4, the fine viscous grid follows the cut labeled as AB in Figure 2. Insofar as the viscous shear layer begins to neck-down shortly behind the base, much of this fine grid resolution is wasted. As a

---

14. *Steger, J.L., Nietubicz, C.J., and Heavey, K.R., "A General Curvilinear Grid Generation Program for Projectile Configurations," ARBRL-MR-03142, U.S. Army Ballistic Research Laboratory, Aberdeen Proving Ground, Maryland 21005, October 1981 (AD A107334).*

consequence, logic has been implemented to adjust the grid cut AB to the viscous shear layer. Such a grid is shown in Figure 5 in which the height of the cut is determined from a moment of shear subject to various constraints and averaging. Specifically, the cut height, $\overline{z}_J$ at each J-location is determined by the relation

$$\overline{z}_J = \frac{\Sigma(\delta_z u_{JL})^2 z_{JL} + \varepsilon D/2}{\Sigma(\delta_z u_{JL})^2 + \varepsilon} \tag{11}$$

where the summation is carried out only for those points within an interval $.2D < Z_{JL} < D/2$. Here D is the base diameter, δ_z is a central difference operator and ε is a positive parameter which ensures a standard grid if all $\delta_z u_{JL}$ are zero or if ε is very large. Additional averaging is used in the x-direction (longitudinal direction). Preliminary results have been obtained using the grid shown in Figure 5 and further computations are underway.

V. RESULTS

The model geometry used in the present study is shown in Figure 6. It consists of a 3 caliber secant-ogive nose and a 3 caliber cylinder.

The free stream Reynolds number for the series of computations was fixed at 4.5×10^6 based on the total model length. The computations were started from free stream conditions and marched in time to obtain the steady state solution. The initial calculation was made for M = 0.9. Previously converged solutions were then used as starting conditions for additional Mach number runs to achieve faster convergence. The results are now presented for both (i) base flow without injection and (ii) base flow with injection.

Figures 7 and 8 show the distribution of the surface pressure coefficient, C_p as a function of axial position without and with mass injection at the base, respectively. The value of C_p beyond X/D = 6 is the value of pressure coefficient along the line extending from the cylinder portion straight to the downstream boundary. When there is no mass injection at the base the pressure distribution in Figure 7 reflects the shock pattern that typically occurs on shell at transonic velocities, the rapid expansion which occurs at the blunt base and the recompression that occurs downstream of the base. The pressure coefficient distribution for a case with large mass addition is shown in Figure 8. The previously observed rapid expansion at the base and recompression downstream of it are seen to be virtually eliminated.

Figure 9 shows the velocity vector field in the base region for M = 0.9, $\alpha = 0$ and $I_j = 0$. Each vector shows the magnitude and the direction of the velocity at that point. The figure shows the velocity field when there is no base bleed and the recirculatory flow in the base region is clearly evident.

The velocity vector plots in Figures 10, 11 and 12 show the effect of base bleed on the near wake flow field. Figure 10 shows the effect of base bleed for the case when the mass injection parameter is very small (I_j = .01). The change in the flow field is not very dramatic. In Figure 11 the mass injection parameter is increased to .07 and the effect of base bleed can be clearly seen. The near wake flow field has changed considerably. Figure 12 shows the effect of base bleed for a higher mass injection parameter, I_j = .13. The flow field in the base region has now been dramatically altered. The recirculation pattern has been totally eliminated.

The next four Figures (13, 14, 15 and 16) are stream function contour plots in the wake region, again for M = 0.9 and α = 0. All these figures are deliberately stretched in y direction (not drawn to the same scale in x and y) to show the flow pattern in the base region as clearly as possible. Figure 13 is for the case of base flow with no mass injection. It clearly shows the recirculation region and the position of the dividing streamline which separates the recirculatory base flow from the main flow. The reattachment point is about 2 calibers down from the base. Note the strong shear layer in the base region.

Figures 14, 15 and 16 show the flow pattern in the base region with mass injection allowed at the base. Figure 14 shows the effect of base bleed when the mass injection parameter is very small (I_j = .01). The reattachment point remains at about the same place as with no injection at the base. The flow pattern has changed slightly as can be seen by the dividing streamline; however, the recirculation region has not changed dramatically. In Figure 15, the mass injection parameter, I_j, has been increased to .07 and now the effect of mass injection can be clearly seen. The reattachment point has moved further downstream. The flow pattern in the near wake flow field has changed considerably and the separation bubble is reduced in size. When the mass injection parameter is increased further, I_j = .13, its effect on the flow field in the base region is apparent. Figure 16 shows that dramatic change in the flow field. The recirculation region has been eliminated and the shear layer has been displaced markedly. Eliminating the recirculation in the wake, increases the base pressure and thus reduces the base drag.

A more critical look at the computational results is presented in Figures 17 through 20. These figures show the quantitative details of projectile flow field. Figure 17 shows the variation of base drag with mass injection rates for M = 0.9 and α = 0. The reduction in base drag with base injection can be clearly seen. The reduction in base drag increases with the increase in the injection rate.

Since the entire projectile flow field, including the base flow, has been computed, all three drag components have been computed and thus the total drag is determined. Figure 18 shows the variation of the total drag with varying mass injection rates. Again, the reduction in the total drag is apparent. As the injection rate is increased, the reduction in total drag increases.

Figures 19 and 20 show, respectively, the variation of base drag and the total drag with Mach number both with and without base injection. In both of

these figures the computational results without base injection are shown by the solid line whereas the dotted line represent the computational results obtained with injection. The reduction in base drag and thus total drag due to base injection can be clearly seen. Figure 19 indicates that the reduction in base drag has increased with an increase in Mach number from .9 to .98 while from M = 1.0 to 1.2, the drag reduction is apparently constant. In both of the figures, the expected drag rise in the transonic speed regime is well predicted for $.9 < M < 1.2$ and the reduction in base drag and the total drag, due to base bleed has been clearly demonstrated.

VI. SUMMARY

A promising computational capability has been developed which computes the full projectile flow field, including the recirculatory base flow, at transonic speeds both with and without base injection.

Numerical computations have been made for Mach numbers $.9 < M < 1.2$ to predict the base drag and the total drag with and without base bleed. Computed results show the qualitative features of the flow field in the near wake for both cases. The effect of base injection on the qualitative nature of base flow has been clearly shown. Quantitative comparisons of base drag and the total drag both with and without base injection have been made with each other. For $M = 0.9$ and $\alpha = 0$ the computational results show the reduction in base drag and the total drag for several mass injection parameters. Results are also presented for $.9 < M < 1.2$ for a given mass injection rate and the reduction in base drag and the total drag has been demonstrated for this range of transonic speeds.

Current efforts are directed at the numerical computation of base flow at supersonic speeds. The encouraging results obtained thus far at transonic speeds indicate that the computational technique shows the promise of predicting the base drag and hence the total drag both with and without base injection. Future computational efforts will investigate the combined effect of boattailing and base bleed on the total aerodynamic drag.

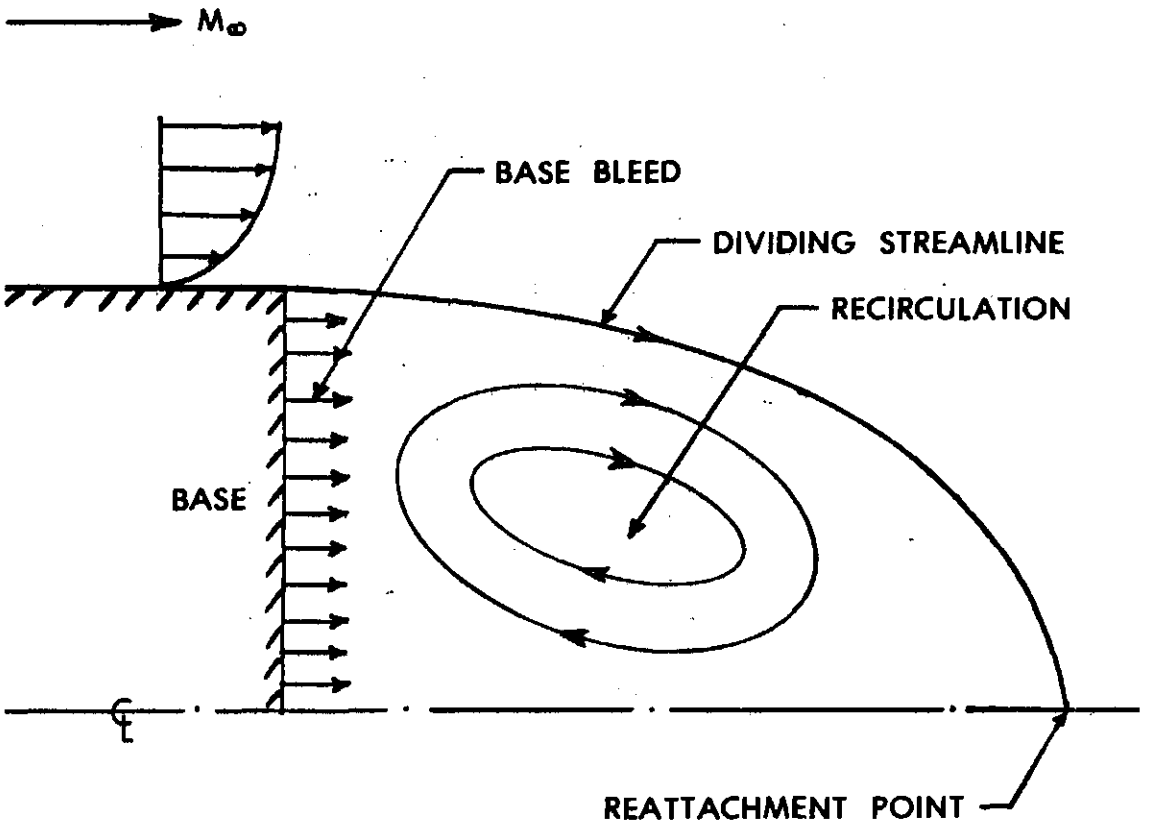

Figure 1. Schematic Illustration of Base Region Flow Field with Base Bleed

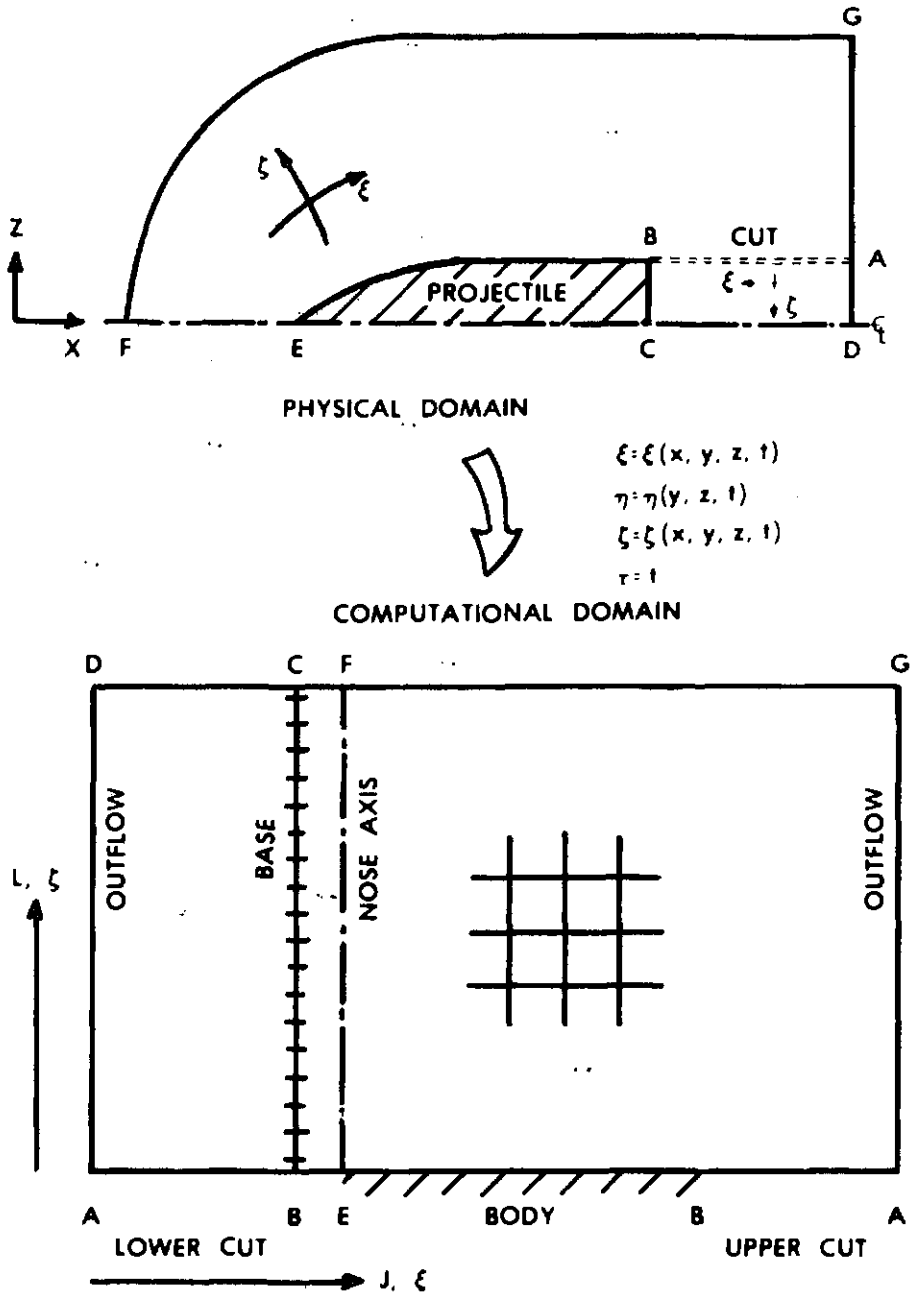

Figure 2. Schematic Illustration of Flow Field Segmentation

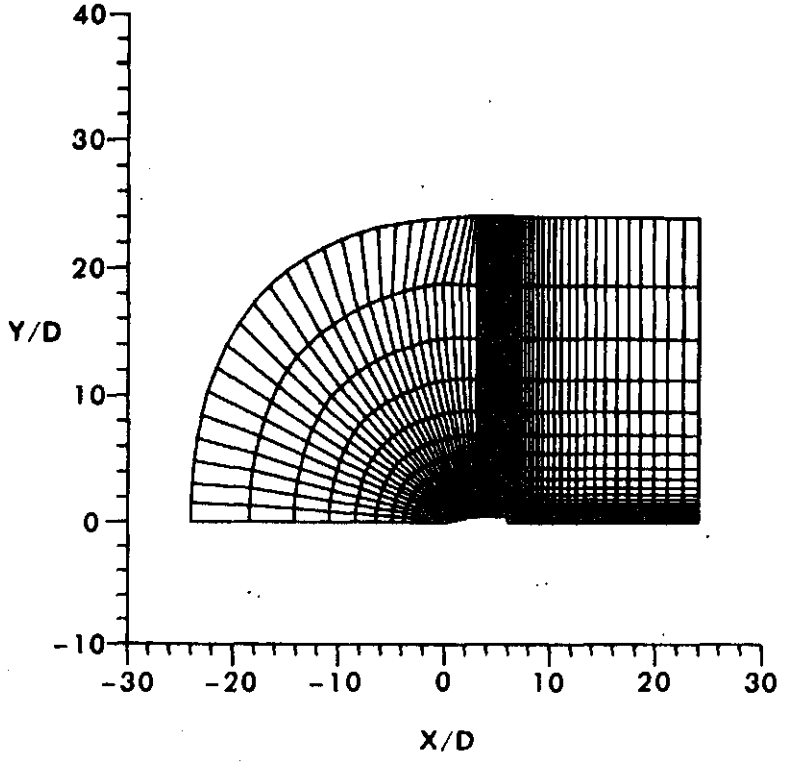

Figure 3. Computational Grid for Flow Field Computations

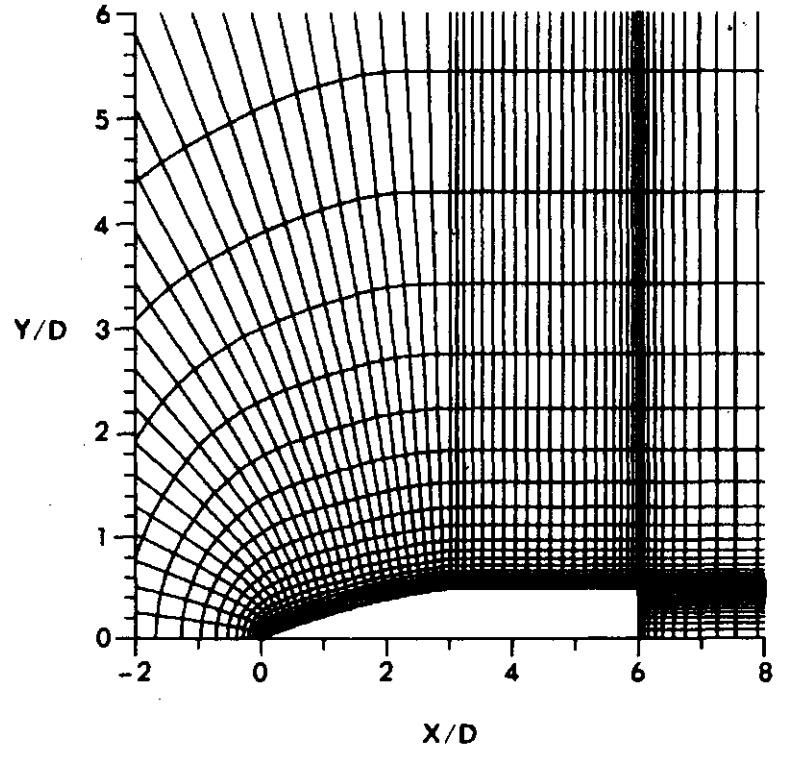

Figure 4. Expanded Grid in the Vicinity of the Projectile

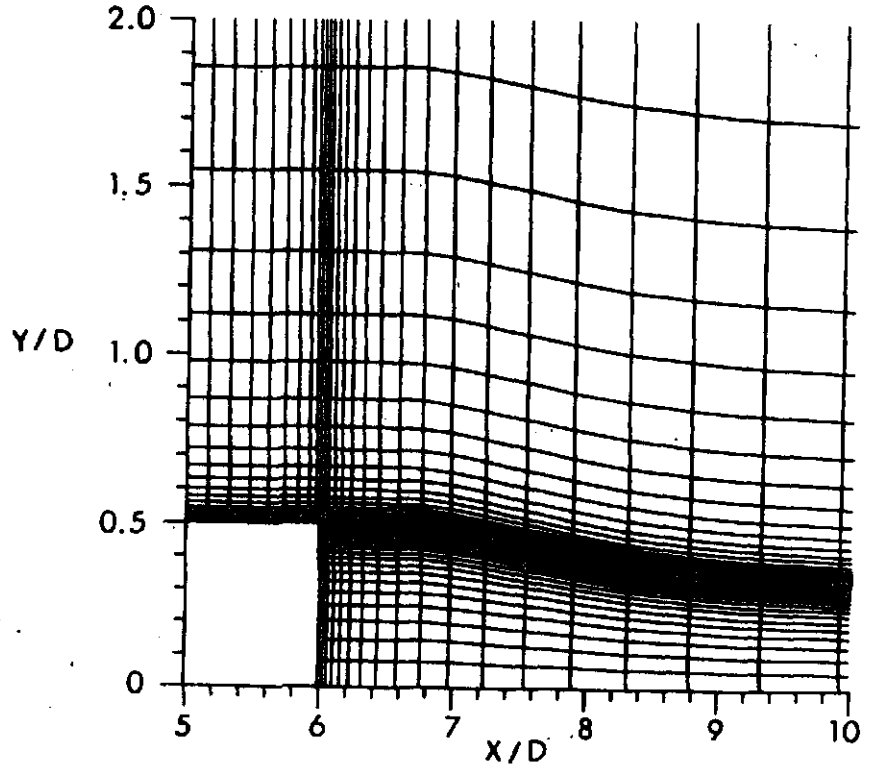

Figure 5. Grid Adapted to the Shear Layer

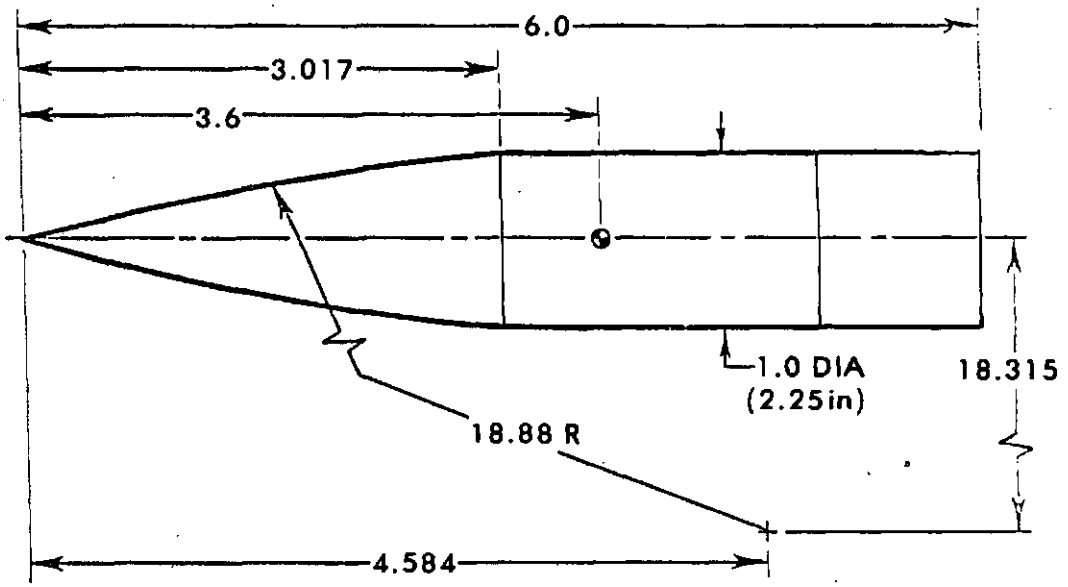

ALL DIMENSIONS IN CALIBERS

Figure 6. Model Geometry

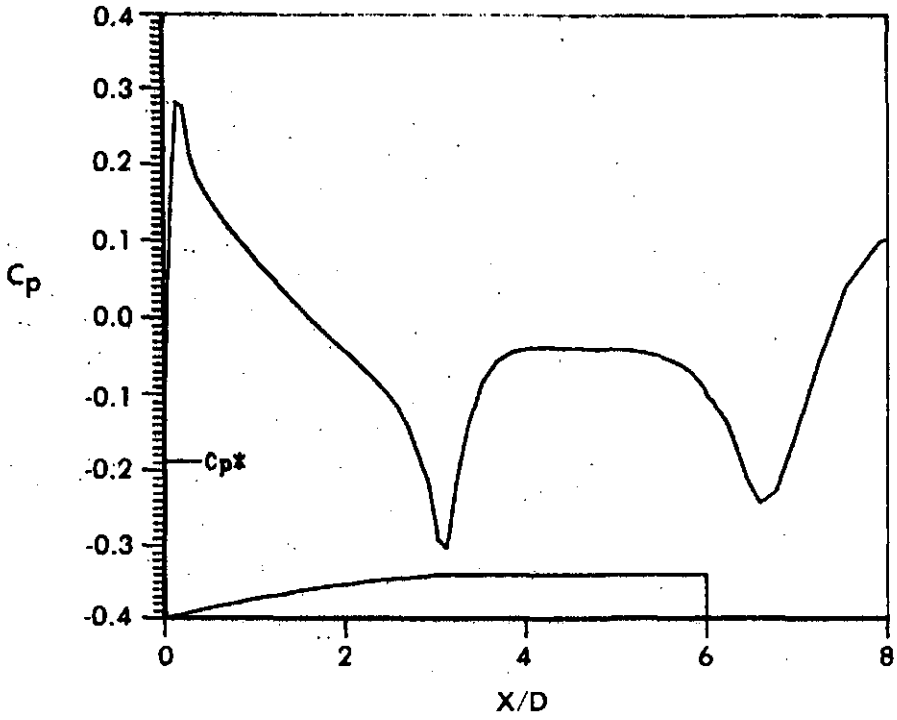

Figure 7. Longitudinal Surface Pressure Distribution, M = 0.9, α = 0, I_j = 0 (without Base Bleed)

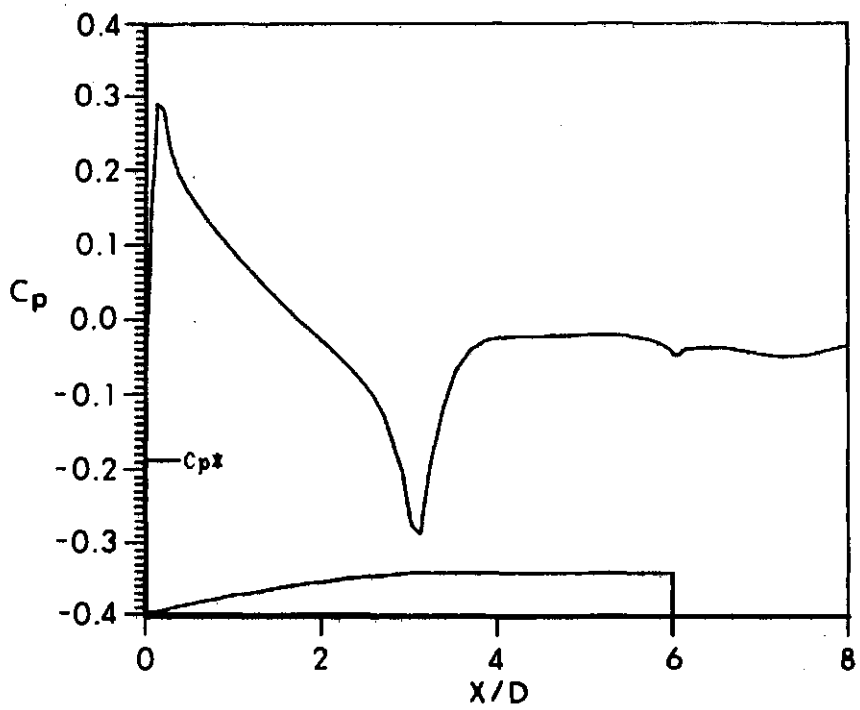

Figure 8. Longitudinal Surface Pressure Distribution, M = 0.9, α = 0, I_j = .13 (with Base Bleed)

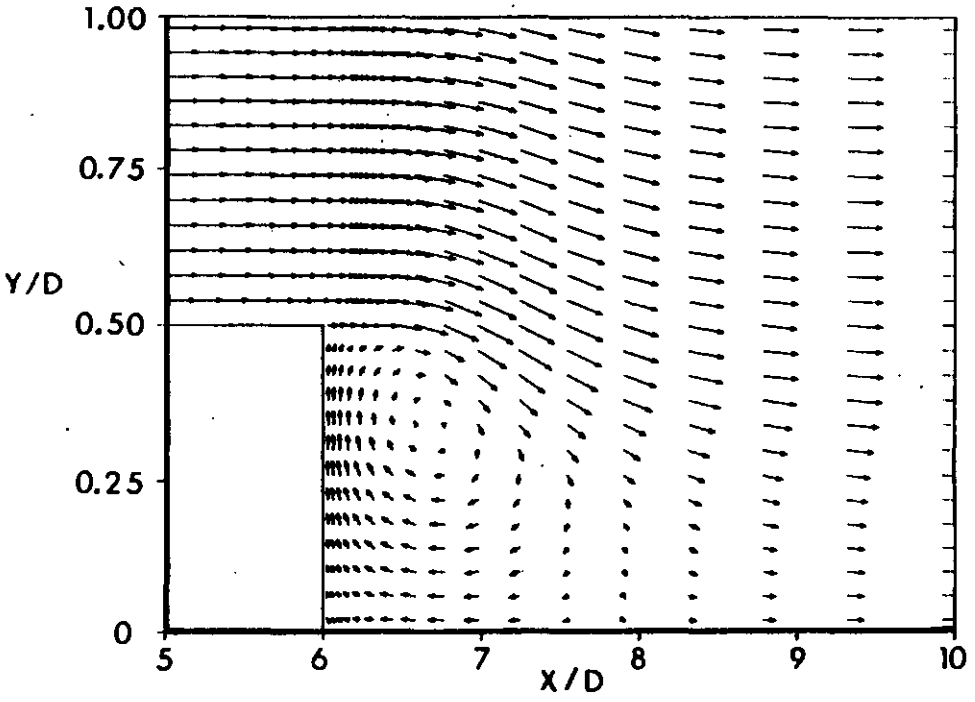

Figure 9. Velocity Vector Field, M = 0.9, α = 0, I_j = 0

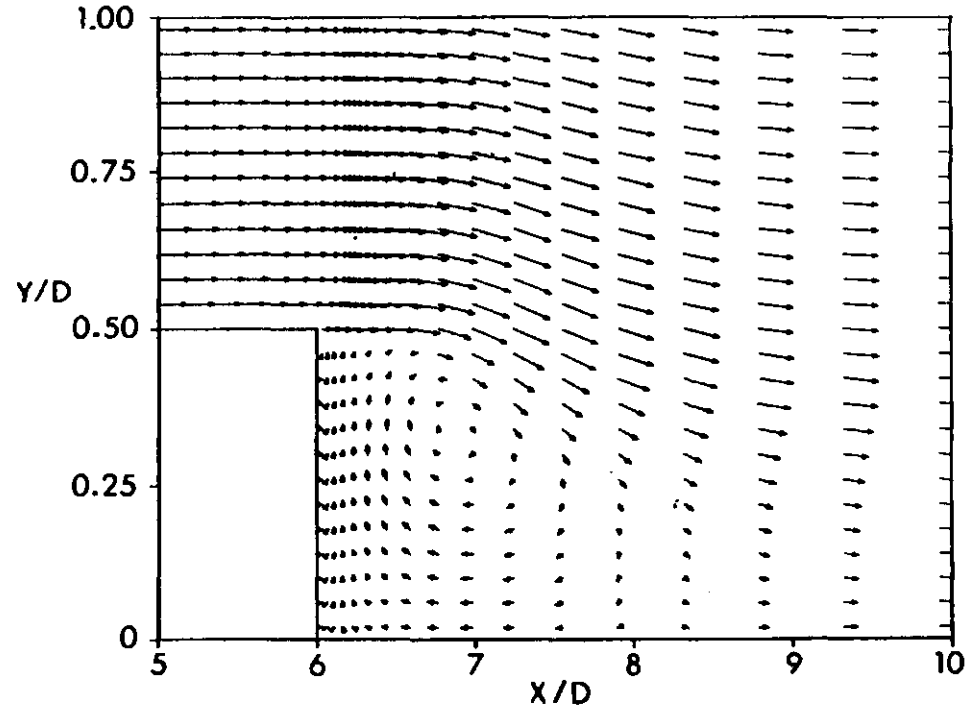

Figure 10. Velocity Vector Field, M = 0.9, α = 0, I_j = .01

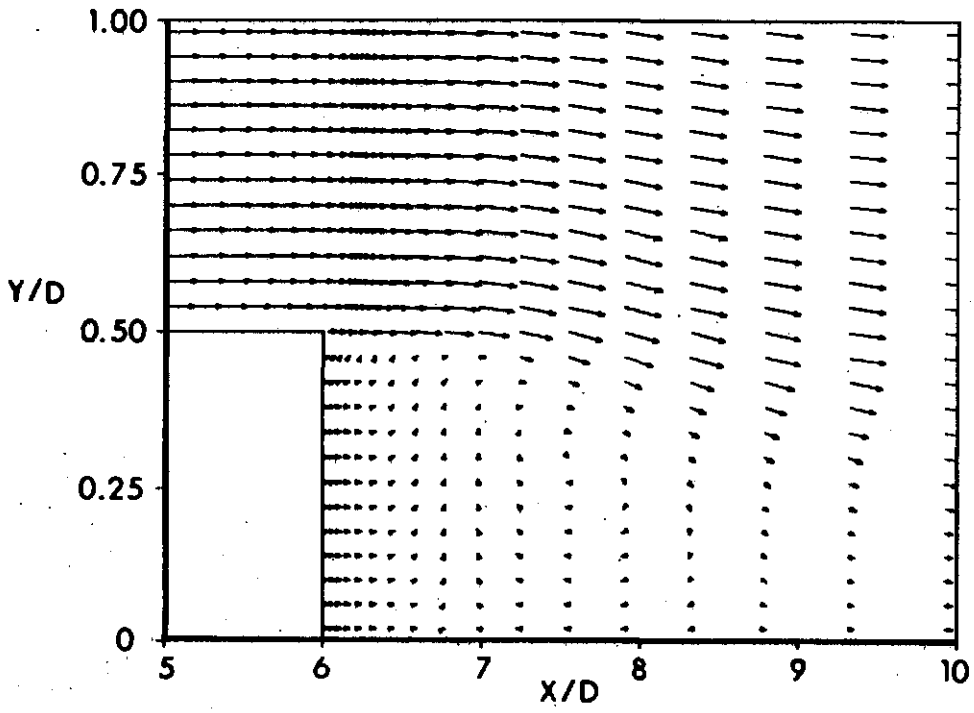

Figure 11. Velocity Vector Field, M = 0.9, α = 0, I_j = .07

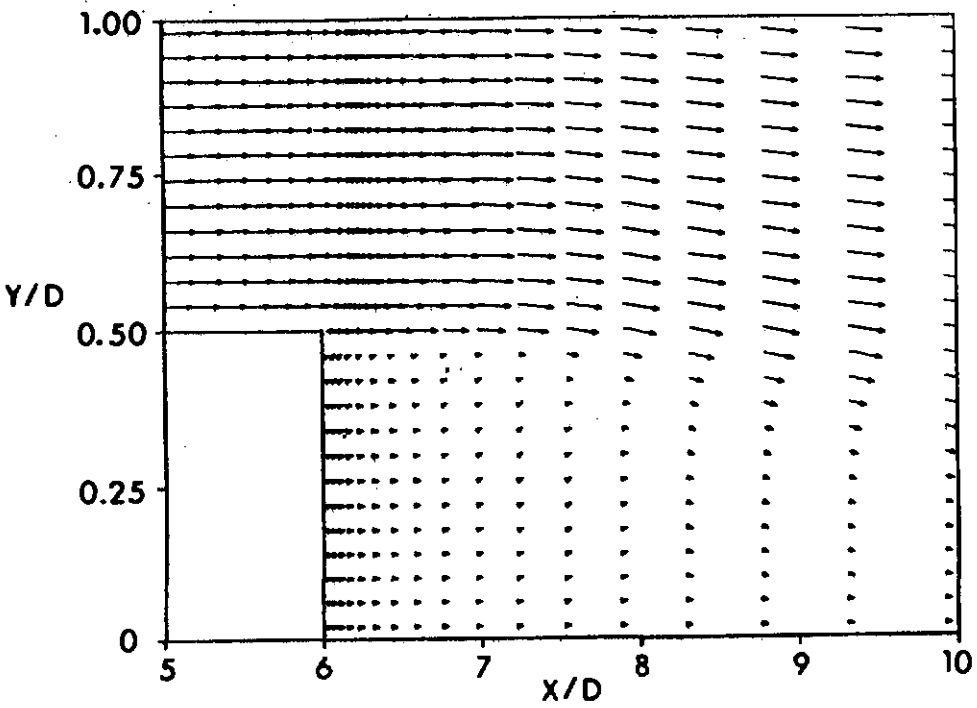

Figure 12. Velocity Vector Field, M = 0.9, α = 0, I_j = .13

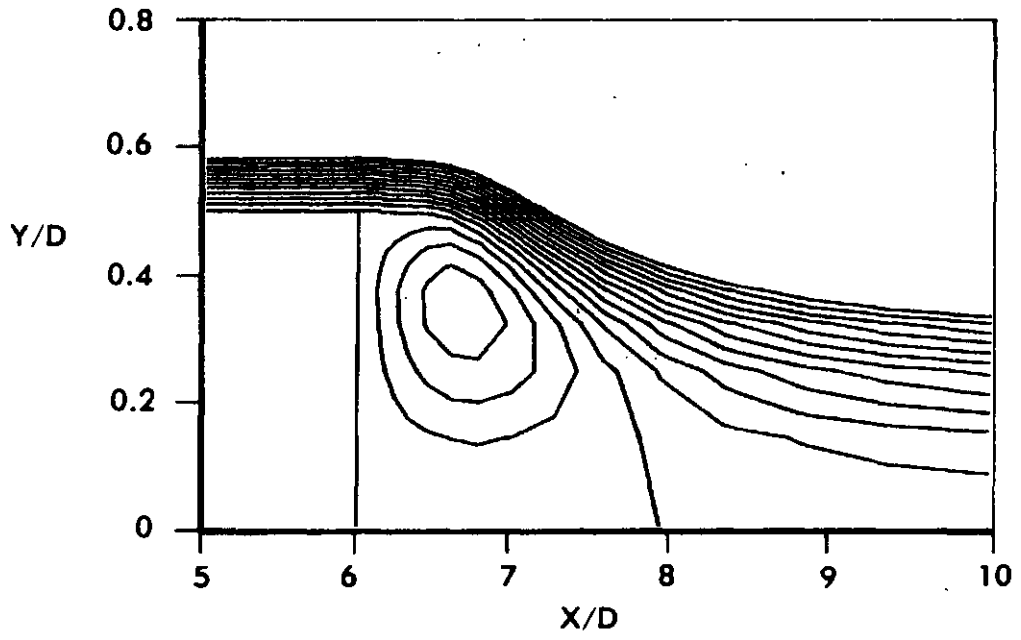

Figure 13. Stream Function Contours, M = 0.9, α = 0, I_j = 0

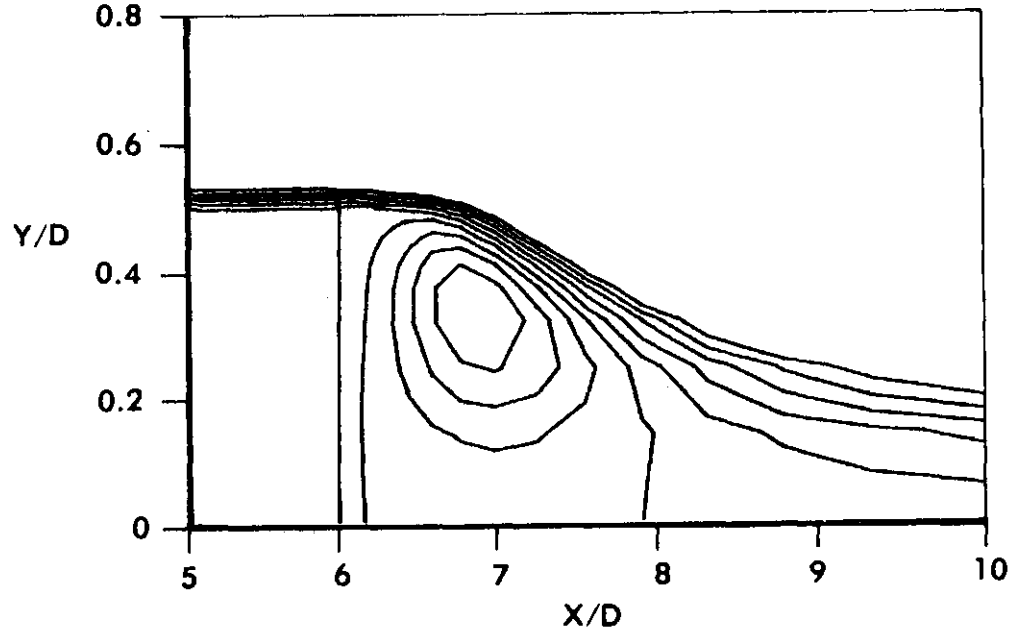

Figure 14. Stream Function Contours, M = 0.9, α = 0, I_j = .01

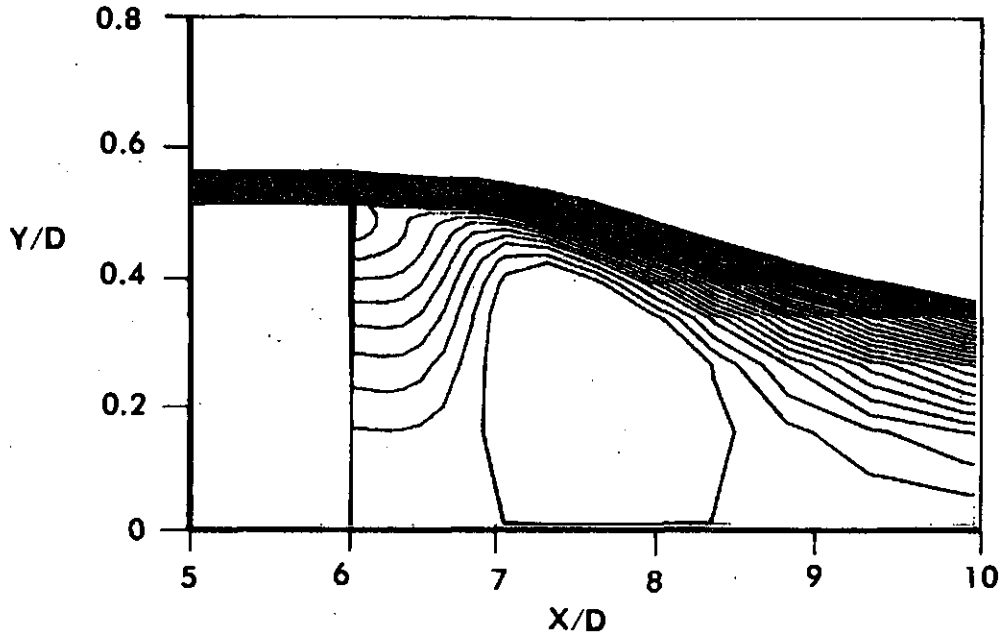

Figure 15. Stream Function Contours, M = 0.9, α = 0, I_j = .07

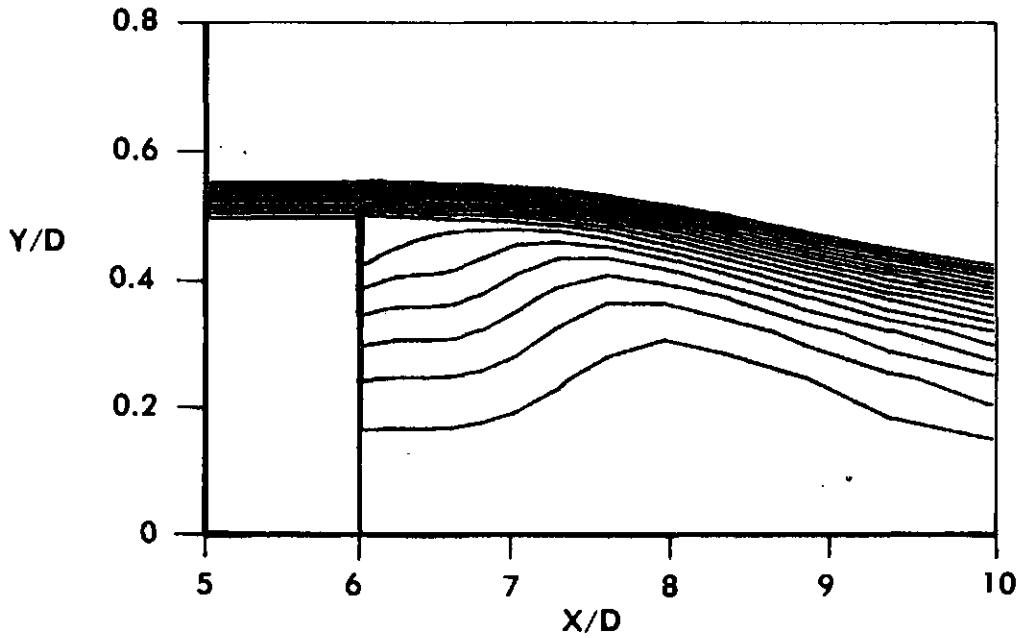

Figure 16. Stream Function Contours, M = 0.9, α = 0, I_j = .13

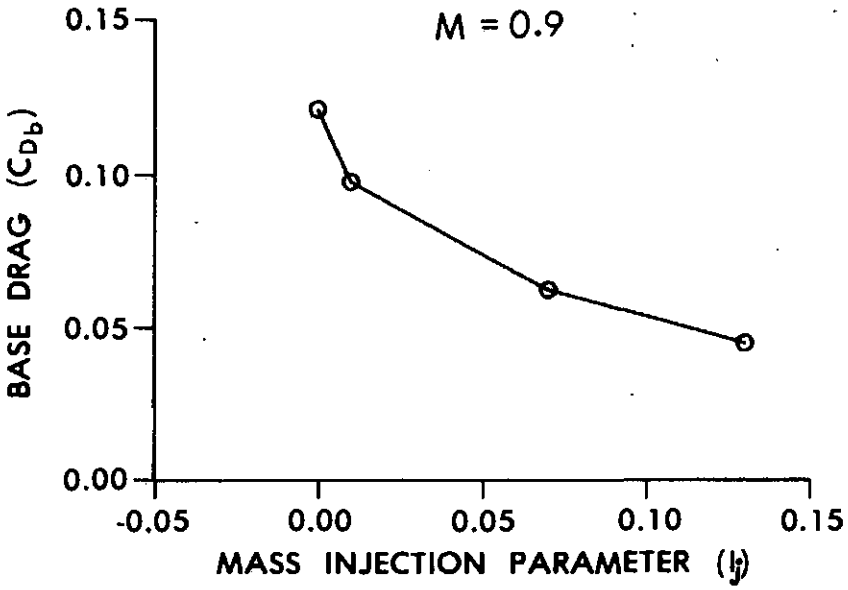

Figure 17. Variation of Base Drag Coefficient with Base Bleed, M = 0.9, α = 0

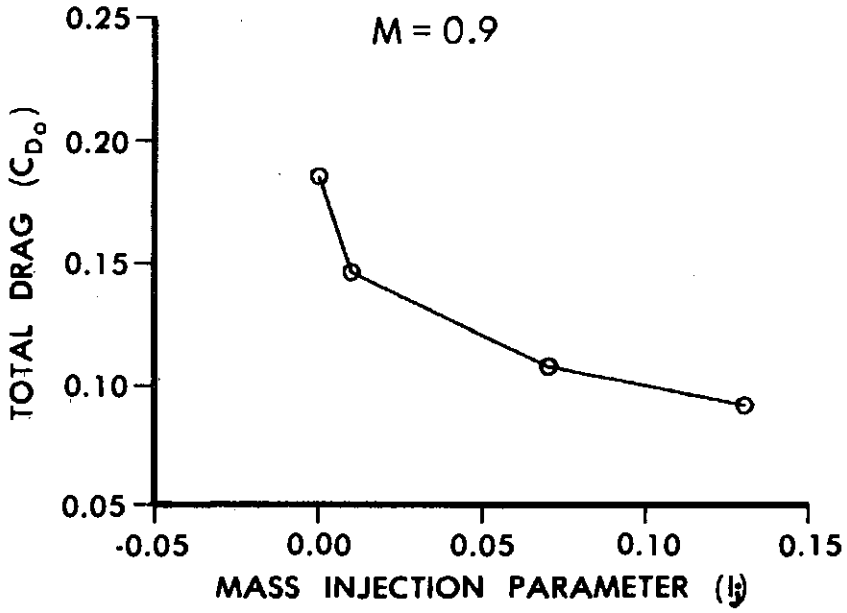

Figure 18. Variation of Total Drag Coefficient with Base Bleed, M = 0.9, α = 0

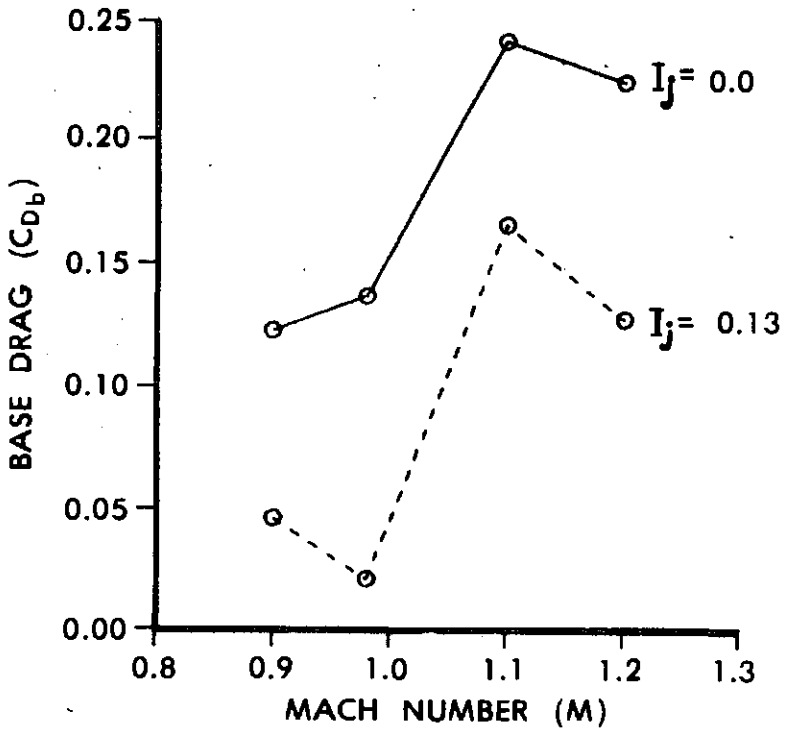

Figure 19. Variation of Base Drag Coefficient with Mach Number, $\alpha = 0$ (with and without Base Bleed)

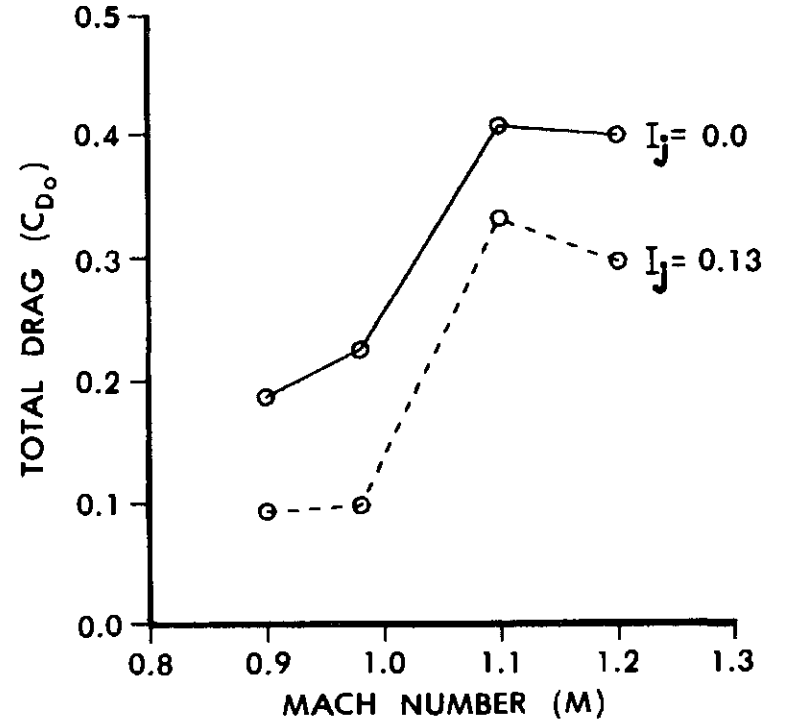

Figure 20. Variation of Total Drag Coefficient with Mach Number, $\alpha = 0$ (with and without Base Bleed)

REFERENCES

1. Sedney, R., "Review of Base Drag," Report No. 1337, U.S. Army Ballistic Research Laboratory, Aberdeen Proving Ground, MD 21005, October 1966 (AD 808767).

2. "155mm ERFB Base Bleed Range and Precision Tests," Conducted at Proof and Experimental Test Establishment, Nicolet, Quebec, for Space Research Corporation, January 11, 1978.

3. Murthy, S.N.B. (Ed.), "Progress in Astronautics and Aeronautics: Aerodynamics of Base Combustion," Vol. 40, AIAA, New York, 1976.

4. Dickinson, E.R., "The Effectiveness of Base-Bleed in Reducing Drag of Boattailed Bodies at Supersonic Velocities," Memorandum Report No. 1244, U.S. Army Ballistic Research Laboratory, Aberdeen Proving Ground, MD 21005, 1960 (AD 234315).

5. Sykes, D.M., "Cylindrical and Boattailed Afterbodies in Transonic Flow with Gas Ejection," AIAA Journal, Vol. 8, No. 3, March 1970, pp. 588-589.

6. Sullins, G.A., Anderson, J.D., and Drummond, J.P., "Numerical Investigation of Supersonic Base Flow with Parallel Injection," AIAA Paper No. 82-1001, June 1982.

7. Nietubicz, C.J., Pulliam, T.H., and Steger, J.L., "Numerical Solution of the Azimuthal-Invariant Thin-Layer Navier-Stokes Equations," ARBRL-TR-02227, U.S. Army Ballistic Research Laboratory, Aberdeen Proving Ground, MD 21005, March 1980 (AD A085716).

8. Nietubicz, C.J., "Navier-Stokes Computations for Conventional and Hollow Projectile Shapes at Transonic Velocities," ARBRL-MR-03184, U.S. Army Ballistic Research Laboratory, Aberdeen Proving Ground, Maryland 21005, July 1982 (AD A116866).

9. Sahu, J., Nietubicz, C.J., and Steger, J.L., "Numerical Computation of Base Flow for a Projectile at Transonic Speeds," ARBRL-TR-02495, U.S. Army Ballistic Research Laboratory, Aberdeen Proving Ground, Maryland 21005, June 1983 (AD A130293).

10. Baldwin, B.S., and Lomax, H., "Thin-Layer Approximation and Algebraic Model for Separated Turbulent Flows," AIAA Paper No. 78-257, 1978.

11. Beam, R., and Warming, R.F., "An Implicit Factored Scheme for the Compressible Navier-Stokes Equations," AIAA Journal, Vol. 16, No. 4, April 1978, pp. 393-402.

12. Steger, J.L., "Implicit Finite Difference Simulation of Flow About Arbitrary Geometries with Application to Airfoils," AIAA Journal, Vol 16, No. 7, July 1978, pp. 679-686.

13. Pulliam, T.H., and Steger, J.L., "On Implicit Finite-Difference Simulations of Three-Dimensional Flow," AIAA Journal, Vol. 18, No. 2, February 1980, pp. 159-167.

REFERENCES (continued)

14. Steger, J.L., Nietubicz, C.J., and Heavey, K.R., "A General Curvilinear Grid Generation Program for Projectile Configurations," ARBRL-MR-03142, U.S. Army Ballistic Research Laboratory, Aberdeen Proving Ground, MD 21005, October 1981 (AD A107334).

LIST OF SYMBOLS

a	speed of sound
a_∞	free stream speed of sound
A	cross-sectional area at the base
A_j	injection area for base bleed
C_{D_b}	base drag coefficient, $2\ D_b/\rho_\infty u_\infty^2 A$
c_p	specific heat at constant pressure
C_p	pressure coefficient, $2(p - p_\infty)/M_\infty^2$
D	body diameter (57.15mm)
D_b	base drag
e	total energy per unit volume/$\rho_\infty a_\infty^2$
$\hat{E}$, $\hat{F}$, $\hat{q}$	flux vector of transformed Navier-Stokes equations
$\hat{H}$	η-invariant source vector
I	identity matrix
I_j	mass injection parameter, $\dot{m}_j/\rho_\infty u_\infty A$
J	Jacobian of transformation
$\dot{m}_j$	mass flow rate for air injection at the base, $\rho_j u_j A_j$
M	Mach number
M_∞	free stream Mach number
p	pressure/$\rho_\infty a_\infty^2$
p_∞	free stream pressure
Pr	Prandtl number, $\mu_\infty C_p/\kappa_\infty$
R	body radius
Re	Reynolds number, $\rho_\infty a_\infty D/\mu_\infty$
$\hat{S}$	viscous flux vector
t	physical time
u,v,w	Cartesian velocity components/a_∞

LIST OF SYMBOLS (continued)

u_∞	free stream velocity
U,V,W	Contravariant velocity components/a_∞
x,y,z	physical Cartesian coordinates
α	angle of attack
γ	ratio of specific heats
κ	coefficient of thermal conductivity/κ_∞
κ_∞	coefficient of thermal conductivity at free stream conditions
μ	coefficient of viscosity/μ_∞
μ_∞	coefficient of viscosity at free stream conditions
ξ,η,ζ	transformed coordinates in axial, circumferential and radial directions
ρ	density/ρ_∞
ρ_∞	free stream density
τ	transformed time
ϕ	circumferential angle
δ	central difference operator
Δ	forward difference operator
∇	backward difference operator

Superscript

*	critical value

Subscript

b	base
j	jet conditions
J	longitudinal direction
L	normal direction
o	total conditions

st	stagnation conditions

This page Left Intentionally Blank

DISTRIBUTION LIST

No. of Copies	Organization
12	Administrator Defense Technical Info Center ATTN: DTIC-DDA Cameron Station Alexandria, VA 22314
1	Commander US Army Materiel Development and Readiness Command ATTN: DRCDMD-ST 5001 Eisenhower Avenue Alexandria, VA 22333
8	Commander Armament Research and Development Center US Army Armament, Munitions and Chemical Command ATTN: DRSMC-TDC (D) DRSMC-TSS (D) DRSMC-LCA-F (D) Mr. D. Mertz Mr. A. Loeb Mr. S. Wasserman Mr. H. Hudgins Mr. E. Friedman Dover, NJ 07801
1	Commander US Army Armament, Munitions and Chemical Command ATTN: DRSMC-LEP-L (R) Rock Island, IL 61299
1	Director Armament Research and Development Center Benet Weapons Laboratory US Army Armament, Munitions and Chemical Command ATTN: DRSMC-LCB-TL Watervliet, NY 12189
1	Commander US Army Aviation Research and Development Command ATTN: DRDAV-E 4300 Goodfellow Blvd. St. Louis, MO 63120
1	Director US Army Air Mobility Research and Development Laboratory Ames Research Center Moffett Field, CA 94035
1	Commander US Army Communications Rsch and Development Command ATTN: DRSEL-ATDD Fort Monmouth, NJ 07703
1	Commander US Army Electronics Research and Development Command Technical Support Activity ATTN: DELSD-L Fort Monmouth, NJ 07703
3	Commander US Army Missile Command ATTN: DRSMI-R DRSMI-RDK Mr. R. Deep Mr. B. Walker Redstone Arsenal, AL 35898
1	Commander US Army Missile Command ATTN: DRSMI-YDL Redstone Arsenal, AL 35898
1	Commander US Army Tank Automotive Command ATTN: DRSTA-TSL Warren, MI 48090
1	Director US Army TRADOC Systems Analysis Activity ATTN: ATAA-SL White Sands Missile Range NM 88002
1	Commander US Army Research Office P. O. Box 12211 Research Triangle Park NC 27709

DISTRIBUTION LIST

No. of Copies	Organization
1	Commander US Naval Air Systems Command ATTN: AIR-604 Washington, D. C. 20360
2	Commander US Naval Surface Weapons Center ATTN: Dr. F. Moore Dr. P. Daniels Dahlgren, VA 22448
4	Commander US Naval Surface Weapons Center ATTN: Code 312 Dr. W. Yanta Mr. R. Voisinet Code R44 Dr. C. Hsieh Dr. R. U. Jettmar Silver Spring, MD 20910
1	Commander US Naval Weapons Center ATTN: Code 3431, Tech Lib China Lake, CA 93555
1	Director NASA Langley Research Center ATTN: NS-185, Tech Lib Langley Station Hampton, VA 23365
3	Director NASA Ames Research Center ATTN: MS-202A-14, Dr. P. Kutler MS-202-1, Dr. T. Pulliam MS-227-8, Dr. L. Schiff Moffett Field, CA 94035
2	Commandant US Army Infantry School ATTN: ATSH-CD-CSO-OR Fort Benning, GA 31905
1	Sandia Laboratories ATTN: Division No. 1331, Mr. H.R. Vaughn Albuquerque, NM 87115
1	AEDC Calspan Field Services ATTN: MS 600 (Dr. John Benek) AAFS, TN 37389
1	AFWL/SUL Kirtland AFB, NM 87117
1	Stanford University Department of Aeronautics and Astronautics ATTN: Prof. J. Steger Stanford, CA 94305
1	University of California, Davis Department of Mechanical Engineering ATTN: Prof. H.A. Dwyer Davis, CA 95616
1	University of Delaware Mechanical and Aerospace Engineering Department ATTN: Dr. J. E. Danberg Newark, DE 19711
1	University of Florida Dept. of Engineering Sciences College of Engineering ATTN: Prof. C. C. Hsu Gainesville, FL 32601
1	University of Illinois at Urbana Champaign Department of Mechanical and Industrial Engineering ATTN: Prof. W. L. Chow Urbana, IL 61801

DISTRIBUTION LIST

No. of Copies	Organization
1	University of Maryland Dept. of Aerospace Engineering ATTN: Dr. J. D. Anderson, Jr. College Park, MD 20742
1	University of Notre Dame Department of Aeronautical and Mechanical Engineering ATTN: Prof. T. J. Mueller Notre Dame, IN 46556
1	University of Texas Department of Aerospace Engineering ATTN: Dr. J. J. Bertin Austin, TX 78712

Aberdeen Proving Ground

Dir, USAMSAA
ATTN: DRXSY-D
DRXSY-MP, H. Cohen

Cdr, USATECOM
ATTN: DRSTE-TO-F

Cdr, CRDC, AMCCOM
ATTN: DRSMC-CLB-PA
DRSMC-CLN
DRSMC-CLJ-L

This page Left Intentionally Blank